Article type: Original Paper

Metamaterial Absorber Integrated Microfluidic Terahertz Sensors

Xin Hu[1], Gaiqi Xu[1,2], Long Wen[1], Huacun Wang[1], Yuncheng Zhao[2], Yaxin Zhang[2], David R. S. Cumming[3], Qin Chen[1,]*

* Corresponding Author: E-mail: qchen2012@sinano.ac.cn

[1]Key Lab of Nanodevices and Applications-CAS & Collaborative Innovation Center of Suzhou Nano Science and Technology, Suzhou Institute of Nano-Tech and Nano-Bionics, Chinese Academy of Sciences (CAS), Suzhou 215123, P. R. China.
[2]Terahertz Science Cooperative Innovation Center, University of Electronic Science and Technology of China, Chengdu 610054, P. R. China
[3]School of Engineering, University of Glasgow, Glasgow G12 8LT, UK

Abstract: Spatial overlap between the electromagnetic fields and the analytes is a key factor for strong light-matter interaction leading to high sensitivity for label-free refractive index sensing. Usually, the overlap and therefore the sensitivity are limited by either the localized near field of plasmonic antennas or the decayed resonant mode outside the cavity applied to monitor the refractive index variation. In this paper, by constructing a metal microstructure array-dielectric-metal (MDM) structure, a novel metamaterial absorber integrated microfluidic sensor is proposed and demonstrated in terahertz (THz) range, where the dielectric layer of the MDM structure is hollow and acts as the microfluidic channel. Tuning the electromagnetic parameters of metamaterial absorber, greatly confined electromagnetic fields can be obtained in the channel resulting in significantly enhanced interaction between the analytes and the THz wave. A high sensitivity of 3.5 THz/RIU is predicted. The experimental results of devices working around 1 THz agree with the simulation ones well. The proposed idea to integrate metamaterial and microfluid with a large light-matter interaction can be extended to other frequency regions and has promising applications in matter detection and biosensing.

1. **Introduction**

Optical sensors are powerful tool for applications including biomedical research, environmental monitoring, and security [1]. They are sensitive, easy to use and immune to electromagnetic interference. In particular, label-free detection for refractive index change is attracting extensive interests [2], including waveguide sensors [3, 4], resonator sensors [5-7], photonic crystal sensors [8, 9], nanowire sensors [10, 11], fiber sensors [12-14], plasmonic sensors [15-17], and metamaterial sensors [18-20]. No matter which type of sensors, the aim is to maximize the interaction between light and analytes. Recently, terahertz (THz) sensing has arisen as a promising technique for biomedical research and matter detection because of the THz fingerprints of DNA molecules and chemical matters [21-24]. Both time-domain and frequency-domain THz spectroscopy have been applied for sensing [25, 26]. However, the widespread use of THz sensing is hampered by the lack of high-performance THz sources and limited sensitivity due to the mismatch between the large wavelengths of THz waves (>30 μm) and the analyte sizes. Great efforts have been made on, for example, spoof plasmon surfaces that support tightly confined electromagnetic surface modes in THz range mimicking surface plasmon in the visible range [27-30], THz antennas that increase molecular absorption cross sections [31-33], THz metamaterial with artificially designed electromagnetic response [34-39], and high-quality (Q) factor THz microstructures [40, 41]. A measured sensitivity of 0.52 THz/RIU was reported around a frequency of 1.7 THz in a prism coupled metal groove array [27]. A higher sensitivity of 1.9 THz/RIU was simulated around a frequency of 11.5 THz due to the Fano resonance in combined gold ring and graphene disk [32]. 1 nm thick ($\lambda/10^6$) thin film detection with 5% resonance peak shift was experimentally demonstrated using extraordinary transmission effect in a sub-10 nm gap in metal film [30]. For liquid sensing, a concentration of kanamycin sulfate as low as 100 picogram/L was similarly demonstrated [39]. A ~~record~~ high Q factor of 500 was reported by guided mode resonance in the THz range [41]. However, the sensitivity is still limited by the weak interaction between analytes with

either the weak near field of plasmonic antennas or the decayed resonant mode outside the cavity. Furthermore, the sensitivity can be greatly reduced in the case that molecules are not attached on the surface as the field intensity quickly decreases with the distance away from the surface. Therefore, it is desired to create strong electromagnetic field with improved spatial overlap with the analytes. Hollow photonic crystal cavities in near infrared were fabricated to achieve this requirement by forming strong cavity resonance in the hollow sample area [5]. It is worth to note that the spatial overlap of an electromagnetic field with an analyte is not always preferred, for example in the case of the lossy analyte that may kill the signal. Carefully balancing between the sensitivity and the signal loss should be considered.

In this paper, a novel metamaterial absorber integrated microfluidic (MAIM) sensor is proposed and experimentally demonstrated in the THz range. Instead of detecting analytes on the surface of metamaterial structure with relatively weak and decayed field distributions, analytes are brought into a channel formed between two parallel metal structures, where transverse cavity resonance appears inside the metal microstructure array-dielectric-metal (MDM) metamaterial absorber. The channel acts as both microfluidic channel and the spacer of MDM metamaterial absorber. Compared to the conventional metamaterial absorber sensors, significant improvement of the sensitivity is obtained because of the greatly enhanced light-matter interaction in the dual-function channel. Furthermore, the metamaterial perfect absorber (MPA) sensor is deep sub-wavelength and angle-independent. The proposed MAIM sensor can be readily extended to other frequency ranges and demonstrates a promising technique for high-sensitivity chemical and bio- sensors.

2. **Mechanism and Design**

The schematic of the MAIM sensor is shown in Fig. 1a, where the metal microstructure array is attached on the cap and the metal reflector is on the substrate. Furthermore, the substrate is etched to form a microfluidic channel by bonding to the cap. The channel height is

controlled by the etch depth of the substrate. THz beam is incident from the cap side and the reflected beam is measured for sensing. The stack of the metal microstructure array, the microfluidic channel and the metal reflector behaves as reflective MDM metamaterial. As well known, by tuning the structure parameters of the MDM metamaterial, a resonant perfect absorption can be observed with the incident wave fully trapped in the spacer between the two metal layers, resulting in a named metamaterial perfect absorber [42-44]. It is very similar to frequency selective surface absorber in microwave [45], where the periodic subwavelength structures are used to manipulate the electromagnetic response. Particularly, the MPA is deep sub-wavelength and angle-independent. Full concentration of electromagnetic field in a subwavelength layer is very attractive for photodetector [46], solar cell [47, 48], modulator [49, 50], etc. In all these cases, the active materials replace the dielectric layers of the MDM and thus have a large overlap with the greatly confined cavity resonance between two metal layers, resulting in significant enhancement of photoelectric conversion or electro-optical response. In contrast, although MPA has been used for sensing [51, 52], the analytes were placed on top of the MDM stack, where the overlap between the electromagnetic field and the analytes are significantly limited because the field is concentrated in the intermediate dielectric layer. By etching away some of the dielectric layer, the sensitivity was improved due to the enlarged overlap between the analyte and the sensing field [53]. In general, the conventional configuration of the MPA sensors as shown in Fig. 1c does not fully exploit the advantage of strong cavity resonance of MPA. In the proposed MAIM device as shown in Fig. 1b, the microfluidic channel is fully overlapped with the resonant field in MPA and therefore leads to improved sensitivity as discussed in the following. Note that microfluidic channels have been fabricated on top of metamaterial [54-56]. In our case, the channel is actually a part of MPA. The unique dual-function channel design provides advantages for THz sensing.

The absorption spectra were calculated numerically by finite-difference time-domain method for the MAIM devices with the model as shown in Fig. 1b, where the cap and the

substrate were assumed as semi-infinite layers, and the microfluidic channel between two metal layers was modeled as a uniform material with the refractive index of the analyte. The sensor with the channel on top of MPA as reported in Ref. 50 and 51 was modeled for comparison as shown in Fig. 1c. The dielectric layer between two metal layers was chosen to be low loss polyimide (n=1.8+i0.06) [41, 57]. The thickness of this layer was optimized to be 2 μm, which gave a nearly perfect absorption peak in a similar frequency region as the MAIM device. Therefore, the MAIM device could be compared with the reference in a similar condition. For both devices, the reflector is aluminium film with a thickness of 200 nm, and the microstructure array consists of crosses in a square lattice with a period P=22 μm, where the long and the short side lengths of both arms of the cross are 15 and 6 μm, respectively. The absorption spectra of the MAIM device and the reference device are shown in Fig. 2a and 2b, respectively. For the MAIM device, a perfect absorption was achieved at the analyte refractive index n=2. For n varying from 2 to 1, the peak absorption decreases but is still above 70% indicating a strong absorption. At the same time, the absorption peak shifts to low frequencies. The peak transmission of the reference device slightly increases with the decreasing n and the transmission peak shows a similar trend of shifting to high frequencies as the MAIM device. As shown in Fig. 2c, both devices have close absorption peaks at n=2, but show large difference at n=1. By linearly fitting the data, the calculated sensitivity of the MAIM device is as high as 3.5 THz/RIU, which is 6 times larger than the reference device. Although the field in Fig. 1e shows a similar distribution to that in Fig. 1d, the microfluidic channel (white dashed box) on top of the MPA has little overlap with the cavity resonant field resulting in a much smaller sensitivity. In contrast, the ~~record~~ high sensitivity of the proposed MAIM sensor benefits from the novel integration of metamaterial and microfluid with a maximum overlap between cavity resonance and analyte. Furthermore, this technique could be extended to other frequency ranges or multi-band sensors by cascading the microstructure array [58].

There are several models in the literatures to explain the mechanism of the MIM MPA including impedance matching model [42-43], vertical interference model [52, 59], and Gap plasmon model [60, 61]. Recently, Zhou et al used a mode expansion method to analytically investigate the resonance in the MIM MPA [62]. It is found that the resonance in such a MDM structure undergoes a transition from a vertical Fabry-Perot type to a transverse type as the spacer thickness reduces. As a result, the vertical interference model was found to give large deviation from the numerical simulation results for thin spacer (<0.3p, p is the period of top metal structure). In contrast, the gap plasmon model, where top metal structure defines the size of the cavity where gap plasmons propagate back and forth, was found to be not applicable for thick spacer [61]. In our case, considering the spacer thickness (1 μm) is less than one twentith of the period (22 μm), it falls in the scope of application of the gap plasmon model. In such a model with transverse resonance, the resonant condition is expressed as [61]

$$4\pi w n_{sp}/\lambda + 2\varphi = 2m\pi \quad (1)$$

where w is the width of the top metal structure, i.e. the cavity length, n_{sp} is the mode index of the gap plasmon, φ is reflection phase, λ is the resonance wavelength, and m is the order of resonance. n_{sp} is depended on the gap size, the spacer and metal dielectric properties [61]. In general, the local variation of the effective index $\Delta n_{sp}(x)$ can be calculated using the overlap integral between the mode field and the change of material refractive index assuming x is the transverse resonance direction [63]:

$$\Delta n_{sp}(x) = \frac{\int\int \Delta n(x, y, z)\left|E(x, y, z)\right|^2 dydz}{\int\int \left|E(x, y, z)\right|^2 dydz} \quad (2)$$

where Δn is the change of the refractive index of analyte in the channel, $|E(x,y,z)|^2$ is the field intensity of the gap plasmon. The integration plane covers both channel and the area above. From Eq. (1) and (2), it is clear that the increase of the analyte index, i.e. the effective index of the gap plasmon, the resonance frequency decreases. Furthermore, because the resonance

inside the channel is larger than that outside, the same change of index inside the channel causes a larger change of the effective index, and therefore a larger resonance frequency shift. This is the reason that our proposed MAIM sensor has higher sensitivity. Similar improvement was demonstrated by partially etching the spacer [52].

To support the analysis above, the on-resonance field and power flux distributions are calculated numerically and shown in Fig. 3. For X-polarized incidence, as shown in Fig. 3a the strong electric field distribution is around two ends of the cross in the X direction, which defines the transverse resonance cavity. As known, the electrical resonance of the top metal structure can induce charges accumulated at the ends of the cross, and these charges induce reverse charges accordingly on the bottom metal reflector. As a result, a strong electrically resonant component in the vertical direction is observed at the two ends of the cross as shown in Fig. 3b, which means that the two metal layers cannot be treated independently. The induced charges result in the reverse surface currents in the two parallel metal layers forming a loop as shown in Fig. 3c. And therefore, the main component of H vector is along the Y direction in the middle of the channel as shown in Fig. 3a. In addition, the calculated power flux as shown in Fig. 3d is clearly along the X direction, indicating a transverse resonance.

3. **Experiments**

The process flow is ~~as~~ shown in Fig. 4a. In the MAIM device, the substrate is used as only a holder and therefore it has plenty of choices. Si wafer was used in the experiment for easy fabrication. Quartz was used as the cap because of its low loss and its transparency for easy monitoring the channel in measurement. Both the substrate and the cap could be polyethylene (PE), polypropylene (PP), polydimethylsiloxane (PDMS) and so on to make the device flexible. The reactive ion etch of Si is a well controllable process to ensure the accuracy of the channel height. The inlet and outlet were fabricated in Si substrate rather than the cap to avoid the possible influence in measurement. Silicon substrate and quartz cap were packaged

together by screws. In most cases, the seal is pretty good due to the flatness of silicon and quartz. Super glue can be used to fully seal the package. Syringe was used to inject the analytes through soft pipes. The reflection spectra were characterized using THz Time-Domain Spectroscopy (THz-TDS) as shown in Fig. S1. The frequency spectrum is then obtained from the time-domain signal via a Fast Fourier Transform. Air (n_{air}=1.00), ethanol ($n_{ethanol}$=1.6), glucose ($n_{glucose}$=2.1) were used as analytes in the experiment, which gives a good spread of refractive index values enabling us to investigate the general performance of the MAIM sensor. Because our THz-TDS system has an upper frequency limit at 1 THz, the low frequency MAIM device was designed and fabricated. The fabricated cross array and the packaged MAIM device are shown in Fig. 4c and 4b. The area of the cross array is approximately 1 cm×1 cm in the center of the device. The incident THz beam can be focused to a 1 mm spot.

As shown in Fig. 5, there is a significant shift of the reflection dip as the varying refractive index of the fluid filling the channel. Experiment results agree with the simulation ones reasonably well. In simulation results shown in Fig. 5a, the absorption dip is at 0.64 THz, 0.79 THz and 0.88 THz for air, ethanol and glucose, respectively. The measured ones shown in Fig. 4b are 0.6 THz, 0.72 THz, 0.82 THz, respectively. The slight discrepancy may be caused by the fabrication error and the simulation parameter error of the analyte indexes. The sensitivity is approximately 0.2 THz/RIU. Because the frequency shift at low frequencies is usually smaller than high frequencies, the sensitivity is normalized to the absorption peak to compare the devices working in different frequency ranges. As a result, the normalized sensitivity is 0.31/RIU (at 0.71 THz). Another device shown in Fig. 5c and 5d has a smaller channel height. It shows similar sensitivity as the one in Fig. 5a and 5b. In addition, the normalized sensitivity of the one in Fig. 2a is 0.55/RIU (at 6.4 THz). In Table 1, recently reported terahertz sensors are compared. The normalized sensitivity of a most recent simulation work is 0.16/RIU (at 11.5 THz) [32] and the normalized sensitivity of an experimental one is 0.3/RIU (at 1.7 THz)

[27]. As seen, the proposed MAIM sensor shows the highest sensitivity of 3.5 THz/RIU in simulation. The experimental results of the MAIM sensor also show a high normalized sensitivity of 0.31/RIU. Note that the proposed MAIM device is compact, angle-independent and easy for parallel integration compared to the one using prism coupling [27]. The device in Reference 17 gives the highest normalized sensitivity of 2.2/RIU. It is worth to mention that Reference 17 and 50 calculate the sensitivity from two analytes with very close refractive index (0.003). In contrast, for general performance estimation the MAIM device was evaluated in a wide refractive index range both numerically and experimentally. With optimization for a certain analyte, the sensitivity of the MAIM device could be further improved.

4. **Discussion**

The cap is found to have an important effect on the performance of the MAIM sensors. First, at a fixed channel thickness, the higher the refractive index of the cap, the smaller the sensitivity. The sensitivity of 3.5 THz/RIU at n_{cap}=1.45 decreases to 0.37 THz/RIU at n_{cap}=3.4 (Supporting information, **S2**). The detailed analysis of the electromagnetic field distributions reveals that the field confinement in the microfluidic channel is stronger at smaller n_{cap}. As a result, the same refractive index variation causes a larger frequency shift. Second, the refractive index of the cap affects the intensity of the reflected signal. In reflection spectra measurements, the THz wave is incident from the cap side. The cap with high refractive index induces substantial reflection from the surface, which weakens the THz beam reaching the analyte in the MAIM sensor and causes dense fluctuations in the spectra due to the interference. Furthermore, the loss of the cap, determined by the imaginary part of the refractive index, causes attenuation of the THz beam, which also reduces the signal intensity. Therefore, a cap with low refractive index and low loss is preferred in the MAIM sensor package.

High frequency (4~9 THz) MAIM sensors were also fabricated and measured by Fourier Transform Infrared spectroscopy (FTIR) (Supporting information, **S3**). A typical device as shown in Figure S3 has a cross array period of 18 μm and the channel height of 1 μm. The long and short side lengths of both arms of the cross are 12 and 6 μm, respectively. The cap was changed to PP, which has a lower refractive index and lower loss in this frequency region than quartz. A high resistivity silicon sample was used to back the PP for package. However, no resonant absorption peak was observed for the packaged device in the FTIR measurement. It is considered that the flexible PP may bend and close the channel resulting in a failure of the device. Two possible ways are proposed to resolve this issue (Figure S4). One is to fabricate silicon pillars during the channel etch in the first step in Fig. 4a. These pillars could support the flexible polypropylene cap and maintain the channel. The other is to spin-coat silicon sample with liquid PP (or PDMS, polyimide), which in all is used as the cap. Good performance can still be expected (Figure S3e).

The overlap of the electromagnetic fields and the analytes in the MAIM sensor can be further improved. Based on the calculated electromagnetic field distributions (Supporting information, Figure S2), there is substantial field at the position of the cap. As a result, the cap could be etched to expose the sides of the metal microstructures, which further increases the interaction between the THz beam and the analyte. 100% improvement of the sensitivity was achieved in simulation (Supporting information, **S4**). In addition, all previously reported MPA in principle can be applied in the proposed MAIM sensor. Therefore, the novel sensor with higher Q-factor and higher figure of merit can be expected with optimization.

5. **Conclusion and Outlook**

A novel microfluidic THz sensor based on metamaterial absorber was proposed and fabricated. A high sensitivity of 3.5 THz/RIU is predicted benefiting from the dual functional microfluidic channel design, where the channel was integrated inside the MDM metamaterial

absorber as a spacer. In contrast to the conventional sensors where only the surface is exposed to the analyte, the resonance field has significantly enlarged overlap with the analyte, and therefore an improved sensitivity. The measured frequency shifts of various analytes within a broad refractive index range agree well with the design, which demonstrates robust feasibility and wide scope of application of the devices. Furthermore, this metamaterial integrated microfluidic sensor can be extended to other frequency ranges and has promising applications in biosensing and matter detection.

In the case of THz sensing, the water absorption is a serious issue. It happens in both the measuring environment and the aqueous solution. Carefully balancing between the strong light-matter interaction (i.e. sensitivity) and the signal loss should be considered. As the frequency shift rather than the amplitude variation is used for sensing in the proposed technique, it may be more robust to the loss issue. However, the water absorption issue has to be addressed in the further development of terahertz sensing.

Supporting Information
Supporting Information is available from the Wiley Online Library or from the author.

Acknowledgements

The authors thank James Grant, Ivonne Carranza and Kevin Gallacher for the Fourier Transform Infrared Spectroscopy measurement. This work is supported by the grants from the National Natural Science Foundation of China (No. 11274344, 11604367 and 61574158), Suzhou Science and Technology Development Program Foundation (No. ZXG201425) and the Royal Society Newton Advanced Fellowship.

Received: ((will be filled in by the editorial staff))
Revised: ((will be filled in by the editorial staff))
Published online: ((will be filled in by the editorial staff))

Keywords: metamaterial, surface plasmon, perfect absorber, microfluid, terahertz sensor

References

[1] S. M. Borisov, O. S. Wolfbeis, *Chem. Rev.* **108**, 423-461 (2008).

[2] X. Fan, I. M. White, S. I. Shopova, H. Zhu, J. D. Suter, Y. Sun, *Analytica Chimica Acta* **620**, 8-26 (2008).

[3] C. F. Carlborg, K. B. Gylfason, A. Kazmierczak, F. Dortu, M. J. B. Polo, A. M. Catala, G. M. Kresbach, H. Sohlstrom, T. Moh, L. Vivien, J. Popplewell, G. Ronan, C. A. Barrios, G. Stemme, W. Wijngaart, *Lab Chip* **10**, 281-290 (2010).

[4] A. Markov, A. Mazhorova, M. Skorobogatiy, *IEEE Trans. Terahz. Sci. Techn.* **3**, 96-102 (2013).

[5] M. R. Lee, P. M. Fauchet, *Opt. Lett.* **32**, 3284-3286 (2007).

[6] A. M. Armani, R. P. Kulkarni, S. E. Fraser, R. C. Flagan, K. J. Vahala, *Science* **317**, 783-787 (2007).

[7] C. Gao, L. Chen, J. Xu, Y. Zhu, *SPIE* **8909**, 89090A-1 (2013).

[8] A. Benz, C. Deutsch, M. Brandstetter, A. M. Andrews, P. Klang, H. Detz, W. Schrenk, G. Strasser, K. Unterrainer, *Sensors* **11**, 6003-6014 (2011).

[9] H. Kurt, M. N. Erim, N. Erim, *Sensors and Actuators B* **165**, 68-75 (2012).

[10] N. S. Ramgir, Y. Yang, M. Zacharias, *Small* **6**, 1705-1722 (2010).

[11] M. Khorasaninejad, N. Abedzadeh, J. Walia, S. Patchett, S. S. Saini, *Nano Lett.* **12**, 4228-4234 (2012).

[12] B. Lee, S. Roh, J. Park, *Optical Fiber Technology* **15**, 209-221 (2009).

[13] S. Feng, S. Darmawi, T. Henning, P. J. Klar, X. Zhang, *Small* **8**, 1937-1944 (2012).

[14] A. Markov, M. Skorobogatiy, *Appl. Phys. Lett.* **103**, 181118 (2013).

[15] J. N. Anker, W. P. Hall, O. Lyandres, N. C. Shah, J. Zhao, R. P. V. Duyne, *Nat. Mater.* **7**, 442-453 (2008).

[16] A. G. Brolo, *Nat. Photon.* **6**, 709-713 (2012).

[17] G. Liu, M. He, Z. Tian, J. Li, J. Liu, *Appl. Opt.* **52**, 5695-5700 (2013).

[18] H. Tao, L. R. Chieffo, M. A. Brenckle, S. M. Siebert, M. Liu, A. C. Strikwerda, K. Fan, D. L. Kaplan, X. Zhang, R. D. Averitt, F. G. Omenetto, *Adv. Mater.* **23**, 3197-3201 (2011).

[19] T. Chen, S. Li, H. Sun, *Sensors* **12**, 2742-2765 (2012).

[20] B. Reinhard, K. Schmitt, T. Fip, M. Volk, J. Neu, A. K. Mahro, R. Beigang, M. Rahm, *SPIE* **8585**, 858507 (2013).

[21] A. Menikh, R. MacColl, C. A. Mannella, X.-C. Zhang, *Chemphyschem* **3**, 655-658 (2002).

[22] M. Nagel, F. Richter, P. Haring-Bolivar, H. Kurz, *Phys. Med. Biol.* **48**, 3625-3636 (2003).

[23] M. Nagel, M. Först, H. Kurz, *J. Phys.: Condens. Matter*. **18**, S601-S618 (2006).

[24] J. F. O'Hara, W. Withayachumnankul, I. Al-Naib, *J. Infrared Milli. Terahz. Waves* **33**, 245-291 (2012).

[25] S. C. Saha, J. P. Grant, Y. Ma, A. Khalid, F. Hong, D. R. S. Cumming, *IEEE T. Thz. Sci. Techn.* **2**, 113-122 (2012).

[26] W. Withayachumnankul, J. F. O'Hara, W. Cao, I. Al-Naib, W. Zhang, *Opt. Express* **22** 972-986 (2014).

[27] B. Ng, J. Wu, S. M. Hanham, A. I. Fernandez-Dominguez, N. Klein, Y. F. Liew, M. B. H. Breese, M. Hong, S. A. Maier, *Adv. Optical Mater.* **1**, 543-548 (2013).

[28] B. Ng, S. M. Hanham, J. Wu, A. I. Fernández-Domínguez, N. Klein, Y. F. Liew, M. B. H. Breese, M. Hong, S. A. Maier, *ACS Photonics* **1**, 1059-1067 (2014).

[29] H. Yao, S. Zhong, *Opt. Express* **22**, 25149-25160 (**2014**).

[30] H.-R. Park, X. Chen, N.-C. Nguyen, J. Peraire, S.-H. Oh, *ACS Photonics* **2**, 417-424 (2015).

[31] H.-R. Park, K. J. Ahn, S. Han, Y.-M. Bahk, N. Park, D.-S. Kim, *Nano Lett.* **13**, 1782-1786 (2013).

[32] Y. Zhang, T. Li, B. Zeng, H. Zhang, H. Lv, X. Huang, W. Zhang, A. Azad, *Nanoscale* **7**, 12682-12688 (2015).

[33] D.-K. Lee, J.-H. Kang, J.-S. Lee, H.-S. Kim, C. Kim, J. H. Kim, T. Lee, J.-H. Son, Q.-H. Park, M. Seo, *Scientific Reports* **5**, 15459 (2015).

[34] H. Tao, A. C. Strikwerda, M. Liu, J. P. Mondia, E. Ekmekci, K. Fan, D. L. Kaplan, W. J. Padilla, X. Zhang, R. D. Averitt, F. G. Omenetto, *Appl. Phys. Lett.* **97**, 261909 (2010).

[35] W. Withayachumnankul, H. Lin, K. Serita, C. M. Shah, S. Sriram, M. Bhaskaran, M. Tonouchi, C. Fumeaux, D. Abbott, *Opt. Express* **20**, 3345-3352 (2012).

[36] B. Reinhard, K. M. Schmitt, V. Wollrab, J. Neu, R. Beigang, M. Rahm, *Appl. Phys. Lett.* **100**, 221101 (2012).

[37] X. Wu, X. Pan, B. Quan, X. Xu, C. Gu, L. Wang, *Appl. Phys. Lett.* **102**, 151109 (2013).

[38] R. Singh, W. Cao, I. Al-Naib, L. Cong. W. Withayachumnankul, W. Zhang, *Appl. Phys. Lett.* **105**, 171101 (2014).

[39] L. Xie, W. Gao, J. Shu, Y. Ying, J. Kono, *Scientific Reports* **5**, 8671 (2015).

[40] C. Jansen, I. A. I. Al-Naib, N. Born, M. Koch, *Appl. Phys. Lett.* **98**, 051109 (2011).

[41] S. Song, F. Sun, Q. Chen, Y. Zhang, *IEEE T. Thz. Sci. Techn.* **5**, 131-136 (2015).

[42] N. I. Landy, S. Sajuyigbe, J. J. Mock, D. R. Smith, W. J. Padilla, *Phys. Rev. Lett.* **100**, 207402 (2008).

[43] X. Liu, T. Starr, A. F. Starr, W. J. Padilla, *Phys. Rev. Lett.* **104**, 207403 (2010).

[44] H.-T. Chen, J. Zhou, J. F. O'Hara, F. Chen, A. K. Azad, A. J. Taylor, *Phys. Rev. Lett.* **105**, 073901 (2010).

[45] W. Xu, Y. He, P. Kong, J. Li, H. Xu, L. Miao, S. Bie, J. Jiang, *J. Appl. Phys.* **118**, 184903 (2015).

[46] S. Song, Q. Chen, L. Jin, F. Sun, *Nanoscale* **5**, 9615-9619 (2013).

[47] L. Wen, F. Sun, Q. Chen, *Appl. Phys. Lett.* **104**, 151106 (2014).

[48] H. Wang, Q. Chen, L. Wen, S. Song, X. Hu, G. Xu, *Photonics Research* **3**, 329-334 (2015).

[49] X. Hu, L. Wen, S. Song, Q. Chen, *Nanotechnology* **26**, 505203 (2015).

[50] Y. Zhang, S. Qiao, S. Liang, Z. Wu, Z. Yang, Z. Feng, H. Sun, Y. Zhou, L. Sun, Z. Chen, X. Zou, B. Zhang, J. Hu, S. Li, Q. Chen, L. Li, G. Xu, Y. Zhao, S. Liu, *Nano Lett.* **15**, 3501 (2015).

[51] N. Liu, M. Mesch, T. Weiss, M. Hentschel, H. Giessen, *Nano Lett.* **10**, 2342-2348 (2010).

[52] B.-X. Wang, X. Zhai, G.-Z. Wang, W.-Q. Huang, L.-L. Wang, *J. Appl. Phys.* **117**, 014504 (2015).

[53] K. Bhattarai, Z. Ku, S. Silva, J. Jeon, J. O. Kim, S. J. Lee, A. Urbas, J. Zhou, *Adv. Opt. Mater.* **3**, 1779 (2015).

[54] W. Withayachumnankul, K. Jaruwongrungsee, A. Tuantranont, C. Fumeaux, D. Abbott, *Sensors and Actuators A: Physical* **189**, 233-237 (2013).

[55] F. Fan, W. Gu, X.-H. Wang, S.-J. Chang, *Appl. Phys. Lett.* **102**, 121113 (2013).

[56] A. Ebrahimi, W. Withayachumnankul, S. Al-Sarawi, D. Abbott, *IEEE Sensors J.* **14**, 1345-1351 (2014).

[57] Y. Ma, Q. Chen, J. Grant, S. C. Saha, A. Khalid, D. R. S. Cumming, *Opt. Lett.* **36**, 945-947 (2011).

[58] Q. Chen, F. Sun, S. Song, *Optics Express* **21**, 15896-15903 (2013).

[59] H.-T. Chen, *Opt. Express* **20**, 7156-7172 (2012).

[60] N. G. Nielsen, D. K. Gramotnev, A. Pors, O. Albrektsen, S. I. Bozhevolnyi, *Opt. Express* **19**, 19310 (2011).

[61] J. Park, J.-H. Kang, X. Liu, M. L. Brongersma, *Sci. Rep.* **5**, 15754 (2015).

[62] S. Ma, S. Xiao, L. Zhou, *Phys. Rev. B* **93**, 045305 (2016).

[63] Z.-Y. Li, D.-X. Xu, W. R. McKinnon, S. Janz, J. H. Schmid, P. Cheben, J.-Z. Yu, *Opt. Express* **17**, 15947-15958 (2009).

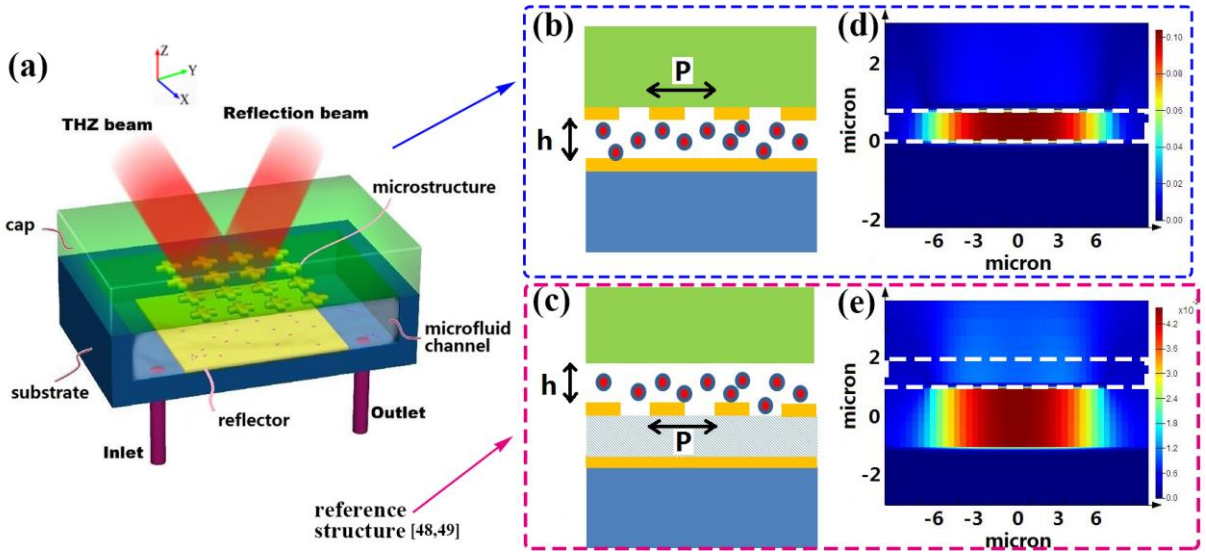

Figure 1. a) Schematic diagram of the MAIM sensor. The microfluidic channel is sandwiched between the metal microstructure array and the metal reflector. The metal microstructure array is attached on the cap and the metal reflector is on the substrate. The analyte in the channel flows in from the inlet and out from the outlet. THz beam is incident from the cap side and the reflected terahertz beam is measured for sensing. b) and c) Schematic diagrams of the cross sections of the MAIM sensor and the reference sensor as Ref. [49,50], respectively. The former has the microfluidic channel inside the MDM stack and the latter has the channel on top of the stack. Circular dots represent the analytes in the channel. d) and e) Resonant magnetic field distributions (intermediate plane along the long arm of the cross) in a unit cell with the refractive index of analyte n = 1.5. The cap (n_{cap}=1.45) and the substrate are assumed as semi-infinite layers. The channel is modeled as a uniform material with a height of h = 1 μm. For both devices, the reflector is aluminium film with a thickness of 200 nm, and the microstructure is a cross array with a period P=22 μm, where the long and short sidelengths of both arms are 15 and 6μm, respectively. For the reference device, the dielectric layer is chosen to be polyimide (1.8+i0.06). The thickness of this layer is set to be 2 μm, resulting in a nearly perfect absorption peak in the similar frequency region. White dashed lines indicate the positions of the channels.

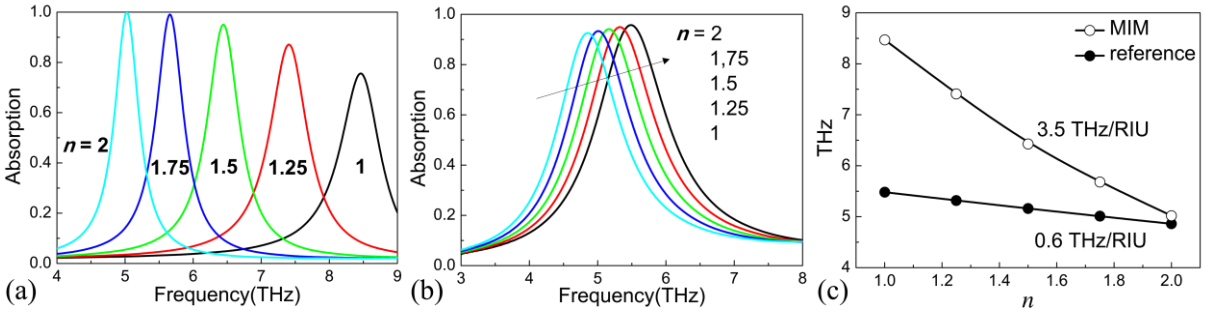

Figure 2. a) and b) are the calculated absorption spectra with refractive index of channel n = 1, 1.25, 1.5, 1.75 and 2 for devices in Fig. 1b and 1c, respectively. c) Resonant peak versus refractive index of analyte for both devices.

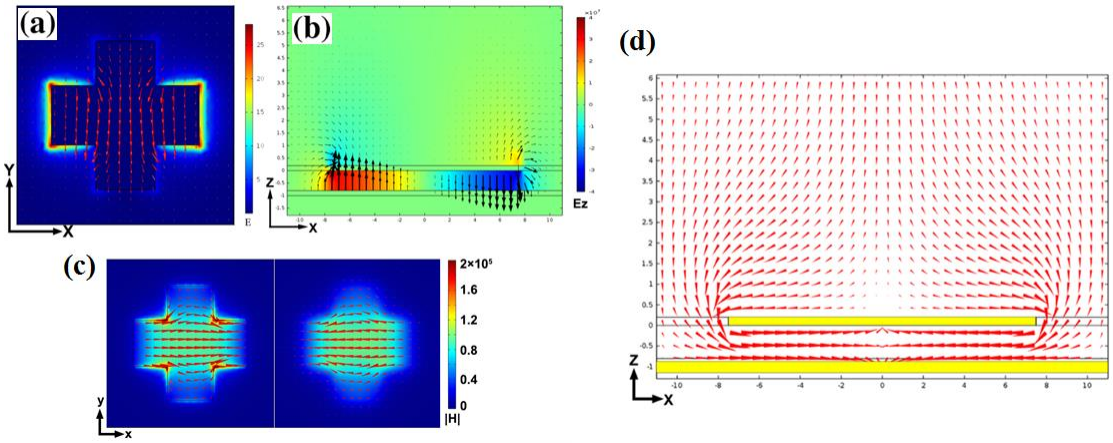

Figure 3. a) |E| distribution overlapped with H vector distribution (red arrows) in the metal cross. b) E vector profile in the X-Z plane passing through the center of the cross. c) Surface current profiles on metal cross and metal reflector. d) Power flux in the same plane as b).

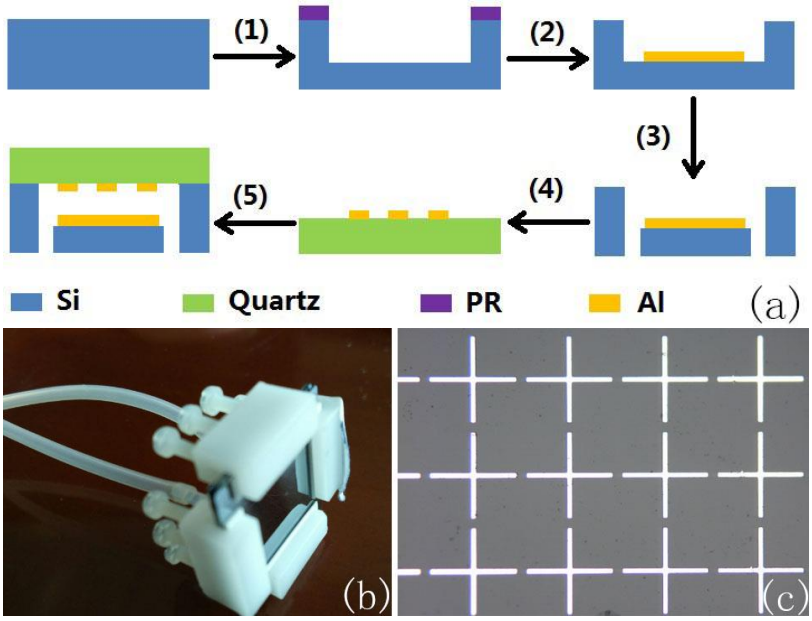

Figure 4. a) Process flow: (1) photolithography and reactive ion etch to form the microfluidic channel in silicon, (2) electron beam evaporation and liftoff to fabricate the reflector, (3) laser drilling to make the inlet and outlet, (4) photolithography and liftoff to fabricate metal microstructure array on quartz, (5) package. Photo images of b) the packaged MAIM device and c) the aluminium cross array. The cross array period P=107 μm. The long and short sidelengths of both arms of the cross are 97 and 6 μm, respectively.

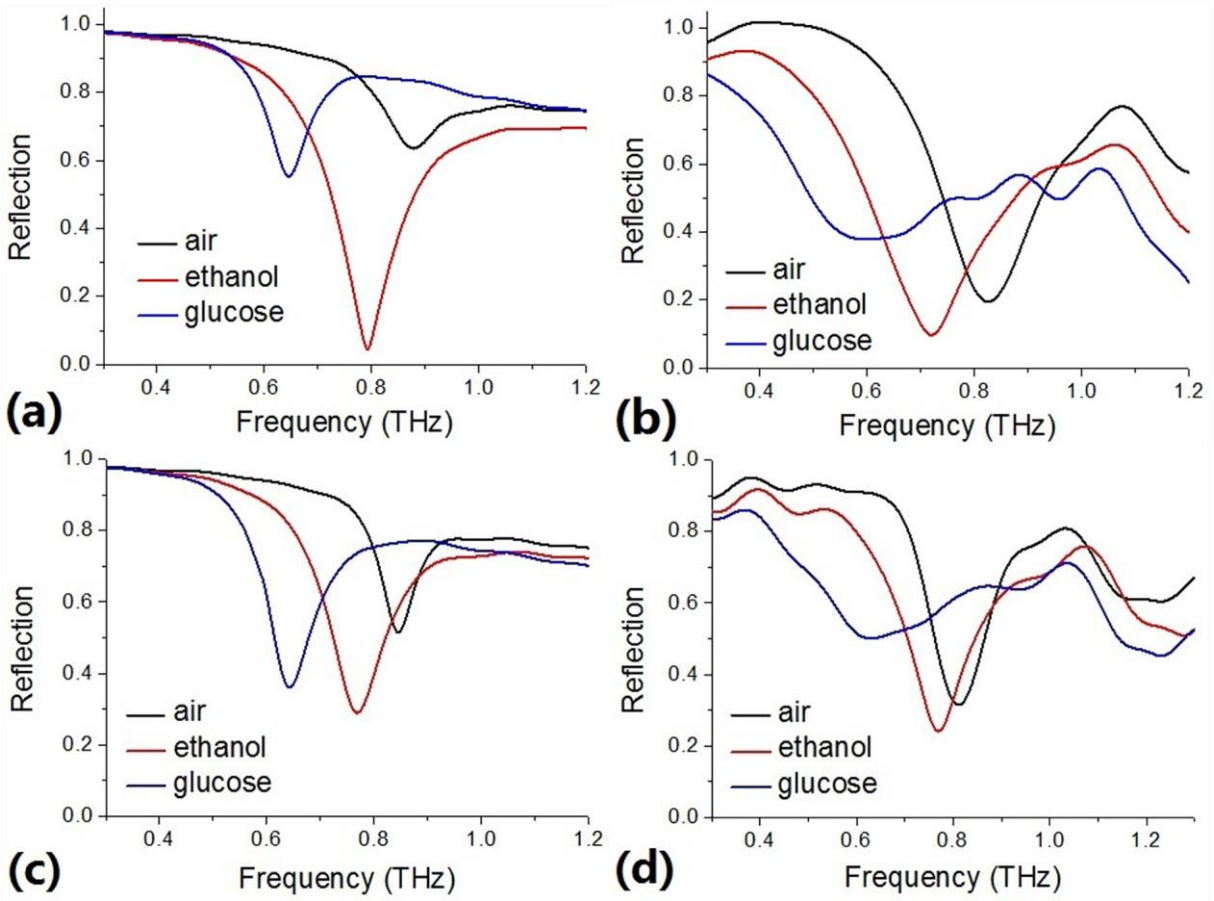

Figure 5. a) and c) Simulation, b) and d) experiment reflection spectra of the MAIM device with air, ethanol and glucose in the channel. 200 nm thick aluminium was used for both reflector and cross array. The period P=107 μm. The long and short sidelengths of both arms of the cross are 97 and 6 μm, respectively. The channel height h=16 μm for (a) and (b), h=12 μm for (c) and (d). In simulation, n_{air}=1.00, $n_{ethanol}$=1.6, $n_{glucose}$=2.1.

Table 1. Comparison of reported THz sensors

Frequency [THz]	Sensitivity [THz/RIU]	Normalized Sensitivity [RIU^{-1}]	Reference	Technique
0.55	0.14	0.25	[7][a)]	Waveguide resonator
0.91	2	2.2	[17][b)]	Metal nanoholes
1.7	0.52	0.31	[27][b)]	Prism coupled nanogrooves
11.5	1.9	0.17	[32][a)]	Metal ring and grapheme disk
0.5	0.04	0.08	[38][b)]	Metamaterial
3.0	1.48	0.49	[50][a)]	Metamaterial perfect absorber
6.4	3.5	0.55	This work[a)]	MPA integrated microfluidic channel
0.71	0.22	0.31	This work[b)]	MPA integrated microfluidic channel

[a)](simulation); [b)](experiment)